In Situ Measurements of the Mechanical Properties of Electrochemically Deposited Li_2CO_3 and Li_2O Nanorods

Hongjun Ye, Siwei Gui, Zaifa Wang, Jingzhao Chen, Qiunan Liu, Xuedong Zhang, Peng Jia, Yushu Tang, Tingting Yang, Congcong Du, Lin Geng, Hui Li, Qiushi Dai, Yongfu Tang,* Liqiang Zhang,* Hui Yang,* and Jianyu Huang*

ABSTRACT: Solid electrolyte interface (SEI) is "the most important but least understood (component) in rechargeable Li ion batteries". The ideal SEI requires high elastic strength and can resist the penetration of a Li dendrite mechanically, which is vital for inhibiting the dendrite growth in lithium batteries. Even though Li_2CO_3 and Li_2O are identified as the major components of SEI, their mechanical properties are not well understood. Herein, SEI related materials such as Li_2CO_3 and Li_2O were electrochemically deposited using an environmental transmission electron microscopy (ETEM), and their mechanical properties were assessed by in situ atomic force microscopy (AFM) and inverse finite element simulations. Both Li_2CO_3 and Li_2O exhibit nanocrystalline structures and good plasticity. The ultimate strength of Li_2CO_3 ranges from 192 to 330 MPa, while that of Li_2O is less than 100 MPa. These results provide a new understanding of the SEI and its related dendritic problems in lithium batteries.

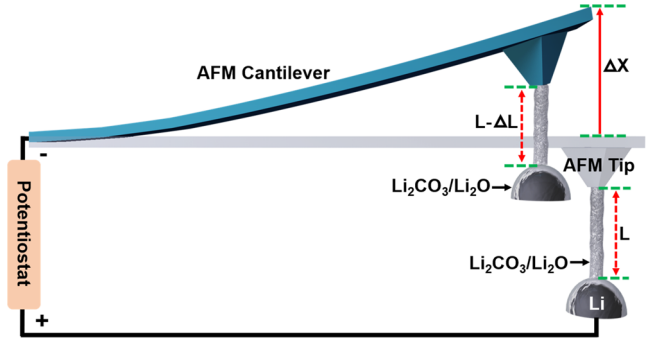

KEYWORDS: *Li_2CO_3 and Li_2O, mechanical properties, in situ environmental transmission electron microscopy (ETEM), atomic force microscopy (AFM), finite element simulations*

INTRODUCTION

Lithium ion batteries (LIBs) have been extensively used in portable electronics and electrical vehicles. When the anode such as graphite or lithium (Li) contacts the electrolyte in LIBs, it reacts with the electrolyte instantly to form a surface layer referred to as solid electrolyte interface (SEI),[1−11] which is considered to be "the most important but least understood (component) in rechargeable Li ion batteries",[4−6] as it is the Li ion transport gateway and always keeps changing during battery cycling.[11] An effective SEI layer can not only protect the anode from further reacting with the electrolyte, thus improving the coulombic efficiency and preventing capacity decay, but also restrict dendrite formation and mitigate short circuits of batteries. It is suggested that the Li dendrite growth may initiate from the pinhole or facture of the SEI layer, which then pierces through the separator or the SEI to reach the cathode, causing a short circuit of LIBs.[3,12,13] Additionally, the fracture of SEI exposes new anode surfaces to the electrolyte, causing a further reaction between the anode and the electrolyte, which leads to electrolyte consumption and capacity decay. Therefore, understanding the mechanical properties of the SEI is critical to improve battery performance and mitigate dendrite growth.[14,15] Nevertheless, there are no in situ transmission electron microscopy (TEM) studies on the mechanical properties of SEI due to the lack of appropriate experimental platforms currently.

It is generally accepted that the SEI is composed of two distinct layers: a thin, dense layer of inorganic species close to the electrode side, and a thick, soft layer of organic and polymeric compounds close to the electrolyte side.[1−10] It is the mechanical strength of the inorganic layer mainly composed of Li_2O, Li_2CO_3, and LiF that plays a critical role in preventing the fracture of the SEI upon cycling and restraining the penetration of Li dendrite, thus mitigating capacity decay and failure of the batteries. However, little is known so far about the mechanical properties of Li_2O, Li_2CO_3, and LiF. Using an aberration corrected environmental transmission electron microscopy (ETEM), we successfully synthesized a series of Li_2CO_3 and Li_2O nanorods and then conducted in situ

measurements to advance our understanding of the mechanical properties of the SEI related materials.

We constructed an electrochemical mechanical device (EMD) comprising a carbon nanotube (CNT) cathode adhered to a conducting atomic force microscopy (AFM) tip, a Li anode, and a naturally formed Li_2O or Li_2CO_3 solid electrolyte.[16,17] It is very difficult to decompose the Li_2CO_3 electrolyte covered on the bulk Li anode under normal electrochemical conditions, which is actully a major issure in the metal−air battery, as with poor electronic (4.4×10^{-9} S·cm^{-1}) and ionic (10^{-7} S·cm^{-1}) conductivity,[18] once the Li_2CO_3 is formed on the surface of the air cathode, it blocks further electron and ion transport of the air cathode, thus shutting off the electrochemical reaction.[19,20] The attachment of the CNT was performed inside the TEM: first, a CNT was aligned with the AFM tip, then the CNT was anchored to the AFM tip by electron beam induced carbon deposition,[21] and finally, the CNT was cut off by the electron beam at the other end opposite to the AFM tip. The growth of Li_2O or Li_2CO_3 nanorods was conducted under an Ar or CO_2 atmosphere, respectively, using the CNT in the EMD as a template. In the O_2 atmosphere, Li_2O_2 was deposited on the surface of the CNT via the reaction $2Li^+ + 2e^- + O_2 \rightarrow Li_2O_2$.[22] In comparison, when Ar was injected into the ETEM column, only a small amount of residual oxygen in the ETEM chamber participated in the reaction, and Li_2O was formed via the reaction $4Li^+ + 4e^- + O_2 \rightarrow 2Li_2O$.[23] When CO_2 was injected into the ETEM column, the Li_2CO_3 formation was attributed to an electrochemical reaction via $4Li^+ + 4e^- + 3CO_2 \rightarrow 2Li_2CO_3 + C$.[20] The CNT acted as a mixed ionic and electronic conductor (MIEC) as reported previously.[24] If we replace CNT with a MnO_2 nanowire, Li_2CO_3 was also deposited on the surface of the MnO_2 nanowire relatively quickly.[20] However, the Li_2CO_3 layer was relatively thin and it was difficult to deposit a thicker Li_2CO_3 layer. The obtained Li_2O or Li_2CO_3 nanorods were then compressed by the piezo manipulator in the EMD for determining their mechanical properties.

EXPERIMENTAL SECTION

Synthesis of Arc-Discharged CNTs. The CNTs used in this study were prepared by an electrical arc method. The anode was an asphalt derived carbon rod, and the cathode was a high purity graphite electrode. To facilitate the collection of CNTs and improve the purity, a wire net was placed on the top of the two electrodes in the chamber and the distance between the wire net and the electrodes was about 5 cm. The buffer gas pressure was set in the range of 0.04−0.05 MPa during the arc discharge experiment; meanwhile, the DC voltage and current for arcing were controlled at 18−20 V and 60−80 A, respectively. By manually advancing the anode that was consumed during the experiment, the distance between the two electrodes was kept at about 1−3 mm.[21]

In Situ Growth of Li_2O and Li_2CO_3 Nanorods. The in situ growth of Li_2O and Li_2CO_3 nanorods were conducted in an aberration corrected ETEM (FEI, Titan G2, 300 kV), which permits gas flows into the sample chamber up to 20.0 mbar. In the experiment, a solid state nanobattery consisting of a Li anode, a Li_2O or Li_2CO_3 electrolyte, and a single nanotube or nanowire as the cathode was set up using a TEM scanning tunneling microscopy (TEM STM) holder (Pico Femto FE F20). A high purity Ar or CO_2 (99.99%) was introduced into the ETEM chamber with a pressure of 1.0 mbar. The generation of Li_2O and Li_2CO_3 was achieved via the electrochemical reactions $4Li^+ + 4e^- + O_2 \rightarrow 2Li_2O$ and $4Li^+ + 4e^- + 3CO_2 \rightarrow 2Li_2CO_3 + C$, respectively.[20,23] The charge and discharge voltages were precisely controlled by a potentiostat (PiciFemto V3ST, produced by Anhui Zeyou Technology Co., Ltd.).

In Situ Characterization of the Deformation Behaviors of Li_2O and Li_2CO_3 Nanorods. To measure the mechanical strength of Li_2O and Li_2CO_3 nanorods, we created a homemade AFM ETEM device, in which a Si AFM cantilever was installed onto one end of the AFM ETEM sample holder. We first welded a short CNT onto the AFM tip by electron beam induced carbon deposition. After that, a piece of Li metal scratched onto an aluminum (Al) tip was mounted onto the other end of the TEM holder (Pico Femto FE F20) inside a glove box filled with dry Ar. Then, the holder was sealed in an airtight bag filled with dry Ar and transferred into the ETEM. The total time of air exposure was less than 2 s, which limited the oxidation of metal Li. Prior to the experiment, high purity CO_2 (99.99%) or Ar (99.99%) was introduced into the specimen chamber with a pressure of 1.0 mbar. Controlled by the piezoelectric tube of the holder, the Li metal attached Al tip can be driven to move toward the AFM tip. When the CNT on the AFM tip and Li metal were connected, an external negative bias was supplied to the AFM tip to facilitate the growth of Li_2CO_3 or Li_2O nanorods. Once the Li_2CO_3 or Li_2O nanorods grew to a certain length, a compression test was carried out by the movement of the piezoelectric tube of the holder toward the AFM tip. The generated force induced not only the deformation in the Li_2CO_3 or Li_2O nanorods but also the deflection of the AFM cantilever, thus permitting real time measurements of the stress caused in Li_2CO_3 or Li_2O. During the experiment, a beam stopper was inserted into the field of view as the reference for displacement measurements of the Li_2CO_3 or Li_2O nanorods and AFM tip. As the AFM cantilever length (520 μm) is much larger than the deflection of the cantilever (<5 μm), a linear relationship between the displacement of the AFM tip ΔX and the force applied on the nanorods F was assumed to be $F = k \times \Delta X$, where k (in the range of 0.1−40 N m^{-1}) is the stiffness of the AFM cantilever that was purchased from the Bruker Company. With the measurements of the diameter and thus the cross sectional area, A, of the Li_2CO_3 or Li_2O nanorods through in situ TEM imaging, the axial compressive stress, σ, generated in the nanorods during compression and the corresponding compressive strength were determined by $\sigma = F/A$. To verify the accuracy of our measurement system, benchmark experiments were conducted by measuring the mechanical strength of individual single crystal Ag pillars.[16] The difference between the results obtained from our AFM ETEM system and a commercial mechanical testing TEM sample holder (Hysitron PI 95) is about ±4.6%, demonstrating the high accuracy of our AFM ETEM testing system. This information was provided in our previous paper.[16]

Identification of Mechanical Properties with Inverse Finite Element Simulations. During the compression test, the nonuniform geometry of the as grown nanorods can lead to the variation of stress distribution in the nanorods. In addition, the compression force always caused localized deformation in the nanorods close to the point that they contact the AFM tip. This is mainly due to the stress concentration of the contact surface and the tapered geometry of the nanorods during compression experiments. To more accurately estimate the mechanical properties of the nanorods, inverse finite element simulations were conducted to simulate the compression behaviors of the nanorods. By systematically tuning the input material parameters to enable the simulation obtained force−compression curve to match the experimentally measured one, the mechanical properties, such as Young's modulus, yield stress, and plastic hardening, can be derived. For simplicity, the elastic−plastic deformation behavior with multilinear isotropic hardening was assumed for all of the nanorods. The models for different nanorods were built referring to their TEM images, and the compressive loading was applied according to the pertinent experimental conditions. To mimic the compression induced bending as well as buckling behaviors of the nanorods, geometric imperfections were introduced into the models via a linear superposition method of the corresponding buckling eigenmodes.

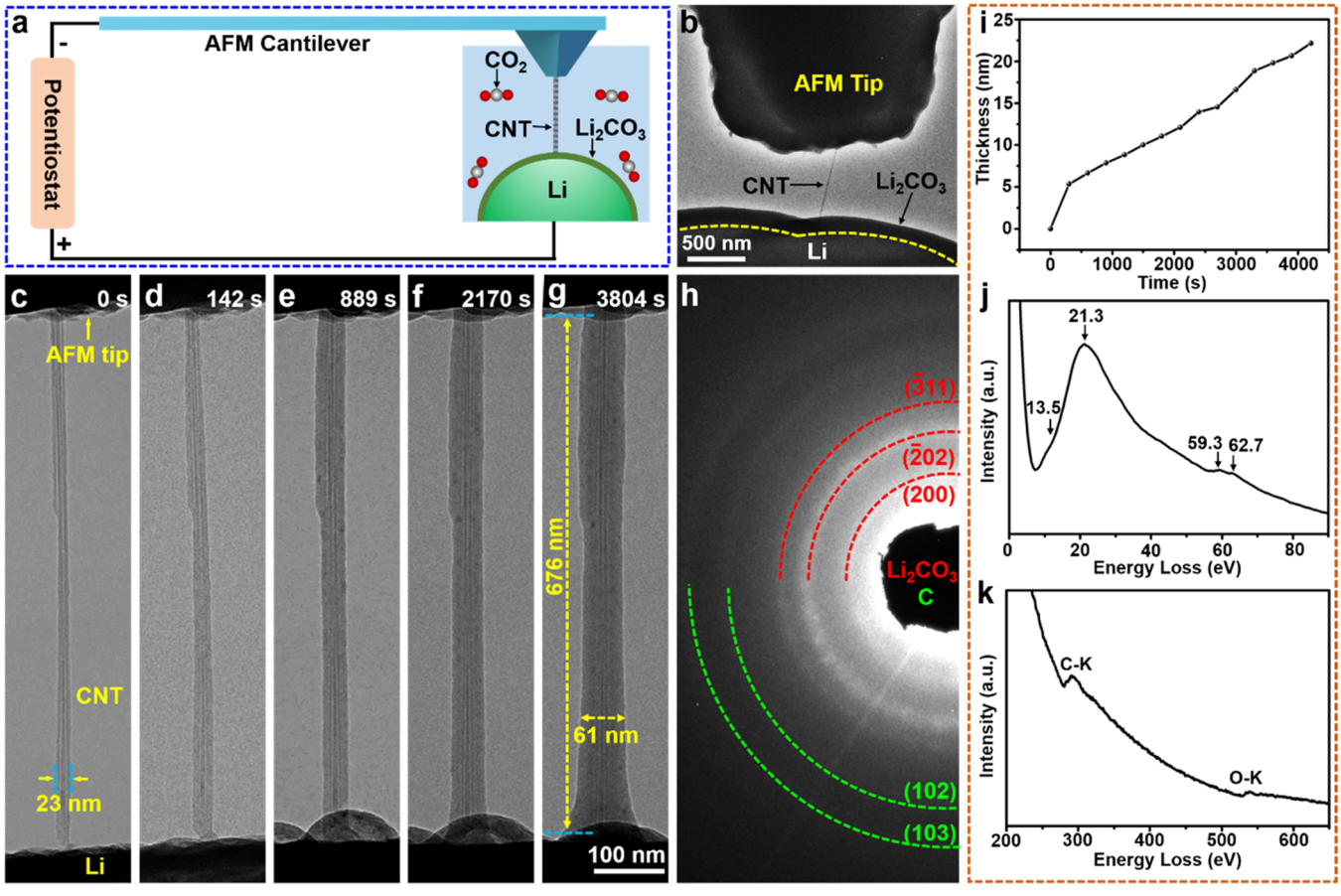

Figure 1. In situ electrochemical growth and characterization of a Li_2CO_3 nanorod. (a) Schematic of the AFM ETEM setup for in situ studies of the mechanical properties of electrochemically deposited Li_2CO_3 nanorods in a CO_2 ambiance. A CNT was attached to the conductive AFM tip by electron beam deposition of carbonaceous material and used as the cathode; a sharp Al needle scratched Li was used as the anode; and the naturally formed Li_2CO_3 on the Li surface was used as an electrolyte. (b) TEM image showing a CNT attached to a flattened AFM tip. (c–g) Time lapse TEM images of a Li_2CO_3 nanorod growth along a CNT by the electrochemical reaction in a CO_2 atmosphere. (h) The selected area electron diffraction (SAED) shows diffraction rings superimposed on a diffused amorphous background, indicating that Li_2CO_3 is polycrystalline with poor crystallinity. (i) Growth rate–time plot of the Li_2CO_3 nanorod. Low loss (j) and core loss (k) electron energy loss spectroscopy (EELS) confirm that the deposited materials are Li_2CO_3. The low loss EELS (j) features a major plasmon peak at 21.3 eV with a shoulder peak at 13.5 eV, both of which are consistent with that of Li_2CO_3.

RESULTS AND DISCUSSION

Figure 1a shows the schematic of the AFM ETEM setup for in situ studies of the mechanical properties of electrochemically deposited Li_2CO_3 nanorods in a CO_2 ambiance. A CNT adhered to a conducting AFM tip by electron beam deposition of carbonaceous material was used as a cathode; a sharp Al needle attached with scratched Li was adopted as an anode; and the naturally formed Li_2CO_3 on the Li surface was used as an electrolyte. As shown in the bright field TEM image in Figure 1b, a CNT was attached to a flattened AFM tip. The time lapse TEM images in Figure 1c–g display a CNT templated growth of a Li_2CO_3 nanorod with a length of 676 nm and a diameter of 61 nm (Figure S1, and Movies S1 and S2 in the Supporting Information).

The formation of Li_2CO_3 is from the following electrochemical reaction: $4Li^+ + 4e^- + 3CO_2 \rightarrow 2Li_2CO_3 + C$.[20] The Li_2CO_3 layer grows intimately onto the CNT with a growth rate increasing linearly with time initially and then slowing down (Figures 1i and S1i). It is difficult for the as grown Li_2CO_3 layer to decompose at room temperature when a reverse bias is applied.[19] The selected area electron diffraction (SAED, Figures 1h, S1e, and S2b) of the nanorod exhibits diffraction rings superimposed on diffuse amorphous background, in which the former is indexed as monoclinic Li_2CO_3 (JCPDS no. 83 1454), and the amorphous background indicates the presence of amorphous materials in the nanorod. The lattice fringes of the high resolution transmission electron microscopy (HRTEM) images of the nanorods are identified as Li_2CO_3 and amorphous carbon (HRTEM, Figure S1f). Electron energy loss spectroscopy (EELS, Figures 1j,k and S1g,h) further confirms that the nanorod is Li_2CO_3. It is worth noting that, according to SAED, the major product is suggested to be Li_2CO_3.

The obtained Li_2CO_3 nanorods were then used for compression tests. Figure 2a shows the schematic of the AFM ETEM setup for in situ compression of the Li_2CO_3 nanorod. When the Li_2CO_3 nanorod is pushed upward by the piezoelectric tube of the holder, the AFM cantilever is bent accordingly with a tip displacement of ΔX, generating a force exerted on the Li_2CO_3 nanorod by the AFM tip to compress it from its initial length of L to $L - \Delta L$, leading to the strain of $\Delta L/L$ in the nanorod. Figure 2b shows a tapered nanorod with the upper and lower diameters of about 338 and 254 nm, respectively. The SAED of the Li_2CO_3 nanorod (Figure S2a)

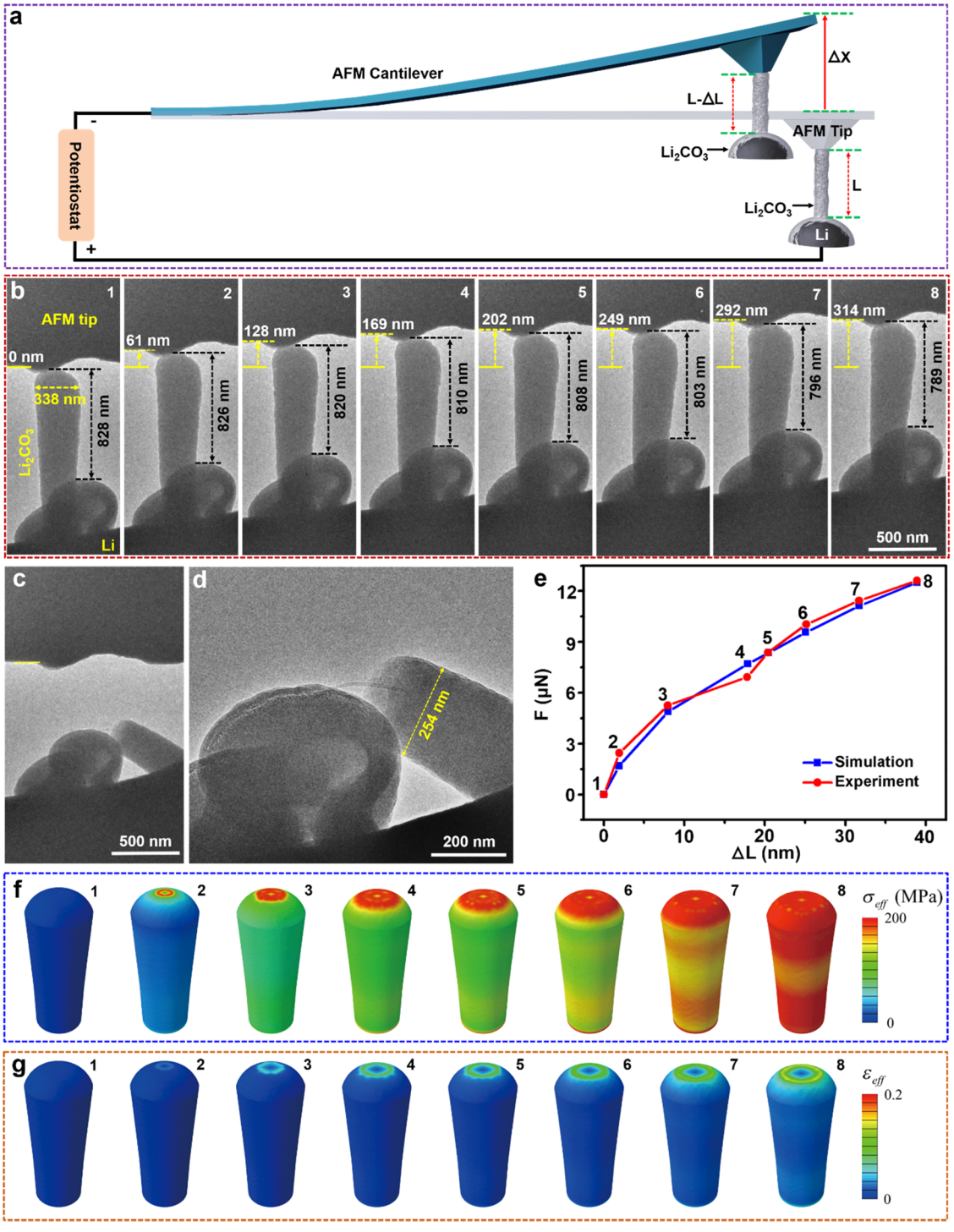

Figure 2. In situ compression of a Li_2CO_3 nanorod and the corresponding simulated stress−strain distributions. (a) Schematic diagram of the AFM ETEM device for in situ compression of the Li_2CO_3 nanorod. (b) In situ compression experiment of a Li_2CO_3 nanorod. (c) The nanorod fractured at the end of compression. (d) High magnification image of the fractured nanorod in (c). (e) Experimental (red) and simulated (blue) force−compression curves of the Li_2CO_3 nanorod shown in (b). Simulated time series snapshots of the effective stress (f) and effective strain (g) contours of the Li_2CO_3 nanorod during compression (corresponding to 1−8 in (b)).

exhibits diffraction rings superimposed on an amorphous background (Figure S2b), and the diffraction rings can be indexed as Li_2CO_3. The dark field image indicates that nanograins are dispersed in the amorphous matrix (Figure S2c). When the nanorod is pushed upward by the piezoelectric manipulator, the AFM cantilever is displaced upward (Figure 2b and Movie S3), forcing the nanorod to be compressed and eventually fractured near the bottom (Figure 2c). As shown in Figure 2d, the inner CNT core is pulled out after fracturing of the nanorod and the surface of the CNT is very smooth, suggesting a sword in sheath failure mode. With the stiffness constant k = 40 N m^{-1} for the Si AFM cantilever, the force F exerted on the AFM tip can be calculated according to Hook's law: $F = k \times \Delta X$.[25] As the amount of compression of the

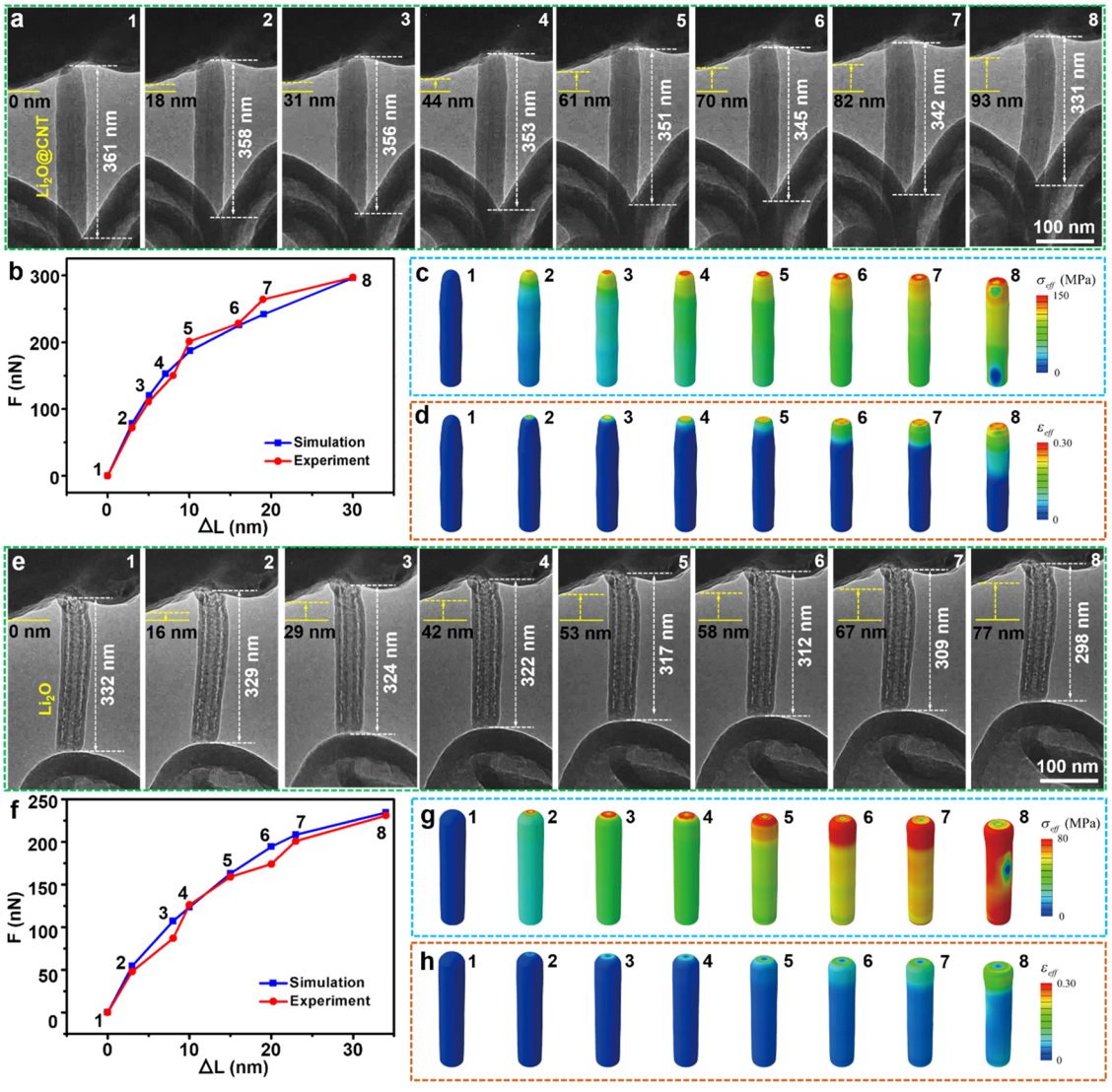

Figure 3. In situ compression tests of Li_2O nanorods and the corresponding simulated stress–strain states. (a) In situ compression test of a Li_2O nanorod. (b) Experimental (red) and simulated (blue) force–compression curves of the Li_2O nanorod shown in (a). Simulated time series snapshots of the effective stress (c) and effective strain (d) in the Li_2O nanorod during compression (corresponding to 1–8 in (a)). (e) In situ compression experiment of a Li_2O nanotube. (f) Experimental (red) and simulated (blue) force–compression curves of the Li_2O nanotube shown in (e). Simulated time series snapshots of the effective stress (g) and effective strain (h) contours in the Li_2O nanotube during compression (corresponding to 1–8 in (e)).

nanorod (ΔL) was directly measured from the TEM images, a force–compression curve, the red curve shown in Figure 2e, can be obtained with the corresponding experimentally measured data provided in Table S1 in the Supporting Information. Based on the geometry of the nanorod and the loading scheme, finite element simulation was conducted to derive the material properties inversely. By tuning the input material parameters, when the stress–strain data listed in Table S2 was adopted, the force–compression curve obtained from the simulation (the blue curve in Figure 2e) can match the experimental one well. The simulated evolutions of the effective stress and effective strain of the Li_2CO_3 nanorod during compression are shown in Figure 2f,g, respectively. It can be clearly seen that the localized stress and strain occurred near the location that the nanorod contacts the AFM tip. With the compression of the nanorod, high level stress and strain appeared in the whole nanorod. Before the fracture of the nanorod, both the top and bottom regions of the nanorod underwent high level stress of up to 192 MPa.

Figure S3 and Movie S4 show the compression test of another short Li_2CO_3 nanorod with a diameter of ~54 nm and a length of ~191 nm. In this case, the inner CNT is already pulled out (Figure S4), leaving an empty core in the nanorod. During the compression test, the nanorod was first compressed (Figure S3a–d) and then bent severely out of the vertical direction (Figure S3d–g). No strain contrast was observed during the compression experiment. After the release of the load, the nanorod retained the bent morphology and the top of the rod was significantly flattened, indicating that the nanorod underwent large plastic deformation during the test. In addition, the nanoscale pores contained in the pristine as deposited nanorod (Figure S1 and Movie S2) disappeared after compression. According to the force–compression curve shown in Figure S3h (with the experimentally measured data listed in Table S3), the force increases almost linearly from

point a to point d, and then almost flatten out from point d to point f due to the bending induced large plastic deformation. Using the force at point d, the ultimate strength can be estimated as ~330 MPa. It should be noted that for this particular nanorod, the CNT was already pulled out, and therefore, its mechanical strength was not affected by the presence of the CNT. The in situ TEM tensile test was performed on the deposited Li_2CO_3 nanorod using the AFM ETEM device. As shown in Figure S5, cracks appear at the bottom of the nanorod when the stretching limit is reached (Figure S5c). The nanorod broke from the crack with further stretching (Figure S5d). The tensile strength of Li_2CO_3 was found to be 188 MPa.

To minimize the electron beam effect, we also conducted compression experiments in the annual dark field (ADF) mode, and a typical example is shown in Figure S6. The nanorod was buckled during compression (Figure S6b) and then fractured into two pieces (Figure S6c), with its cross section clearly visible (Figure S6d,f). Such large buckling of the nanorod again indicates good plasticity of the as deposited Li_2CO_3 nanorod. The SAED (Figure S6g) shows weak diffraction rings superimposed on a strong amorphous background, suggesting poor crystallinity of the nanorod.

Adopting a similar approach to grow Li_2CO_3 nanorods, Li_2O nanorods were also synthesized by electrochemical deposition in an Ar atmosphere (Figure S7a–e and Movie S5). The obtained Li_2O was confirmed by SAED (Figure S7f) and EELS (Figure S7g,h). The SAED (Figure S7f) can be indexed as cubic Li_2O (JCPDS no. 77 2144). The low loss EELS (Figure S7g) features three peaks at 10.5, 18.5, and 30.1 eV, which are consistent with those of Li_2O.[26] The presence of two characteristic peaks at 59.1 and 63.5 eV (Figure S7g) indicates the presence of Li_2O.[26−29] The core loss EELS (Figure S7h) displays the C−K and O−K edges. The Li_2O layer grows intimately on the CNT with a growth rate increasing almost linearly (Figure S7i). The growth of Li_2O can be attributed to the following electrochemical reaction: $4Li^+ + 4e^- + O_2 \rightarrow 2Li_2O$, and the O_2 is from the residue gas in the TEM column.[23]

The as synthesized Li_2O nanorods were then subjected to compression. Figure 3a and Movie S6 show the compression behavior of one of the nanorods. The nanorod was compressed uniaxially first and then bent slightly (Figure 3a 8) due to its geometric imperfections and the high aspect ratio (7.2). The experimentally measured force−deformation data and the corresponding force−compression curve are provided in Table S4 and Figure 3b, respectively. To derive the material properties of the nanorods, finite element simulations were conducted. By matching the simulation obtained force−compression curve (blue) with experimentally measured one (red), as shown in Figure 3b, the stress−strain data for the Li_2O nanorod with an inner CNT core were extracted, as listed in Table S5. Figure 3c,d shows the simulated time series snapshots of the effective stress and effective strain, respectively. Again, the compression always led to localized stress and strain near the region that the external loading was applied. At a point when the nanorod started to bend (Figure 3a 8), the maximum compression induced stress was 111 MPa, which could represent a low bound of the maximum stress that the nanorod could sustain, as serious buckling of the nanorod could still be caused without any failure if the nanorod was continuously compressed, as shown in Figure S8c. If we pulled back the nanorod, it stuck to the AFM tip (Figure S8d–f) and eventually broke from the bottom with the inner CNT being pulled out, forming a Li_2O nanotube with a wall thickness of about 28 nm (Figure S8f). The tensile strength of the Li_2O nanorod was estimated to be 249 MPa. As the tensile strength of a CNT is much higher than that of the Li_2O, the pulling out process can be considered as a sword in sheath manner,[30] i.e., the Li_2O was the sheath while the CNT was the sword. It is interesting to note that with the continued electron bombard ment, a circumferential gap emerged in the Li_2O wall (Figure S8d), which propagated downward the nanorod and eventually extended over the entire Li_2O tube wall, forming a double shelled tubular structure (Figure S8f–i). The formation of the gap in the Li_2O may be ascribed to the stress generated by the pulling out of the CNT and electron bombardment but the exact reason warrants further investigation.

After pulling out the inner CNT, a compression test was then conducted on the double shelled Li_2O nanotube (Figure 3e and Movie S7). In sharp contrast to the compression of the Li_2CO_3 nanorod, the Li_2O nanotube displayed good flexibility and did not fracture even after severe buckling, suggesting excellent plasticity of the Li_2O nanotube. The experimentally measured force−deformation data and the corresponding force−compression curve are provided in Table S6 and Figure 3f, respectively. By matching the finite element simulated force−compression curve with the experimentally measured one (Figure 3f), the stress−strain data for the Li_2O nanotube were derived, as listed in Table S7. The corresponding simulated time series snapshots of the effective stress and effective strain are presented in Figure 3g,h, respectively. Considering that the compression process of the nanotube occurred before serious buckling (Figure 3e 8), the simulated largest effective stress in the nanotube was 77 MPa.

Li_2O is one of the leading candidates for the breeding material in a fusion reactor blanket. Its mechanical properties strongly depend on the porosity. According to the previous publications,[31] Young's modulus of Li_2O increases from ~72 to ~114 GPa when its density increases from 81.4 to 91.5% of its theoretical density, and the compressive strength of Li_2O with 81.4 and 91.5% of the theoretical density is about 132 and 139 MPa, respectively.[31] In addition, Young's modulus and shear modulus of coarse grained Li_2O with a grain size of ~40 μm and a theoretical density of 90% are 108 and 45.6 GPa, respectively.[32] Considering the fact that the electrochemically deposited Li_2O possesses the porous composite structure with nanograins dispersed in the amorphous matrix, the derived mechanical properties of our electrochemically deposited Li_2O nanorods are still reasonable.

For Li_2CO_3, based on the molecular dynamics simulation, the shear modulus of amorphous Li_2CO_3 is about 8 GPa at room temperature.[33] Shin et al. calculated the shear modulus of crystalline and amorphous Li_2CO_3 to be 22.2 and 13 GPa, the bulk modulus of crystalline and amorphous Li_2CO_3 to be 50.5 and 43.1 GPa, respectively.[34] Based on Pugh's criterion (B/G ratio, bulk modulus/shear modulus) of a brittleness material,[35] the Li_2CO_3, irrespective of crystalline or amor phous, is a ductile material (>1.75).[34] If we consider the shear modulus of amorphous Li_2CO_3 as 8 GPa, the theoretical strength can be estimated as one tenth of the shear modulus, which is about 800 MPa. In this study, the derived mechanical strength of electrochemically deposited Li_2CO_3, which ranges from ~192 to ~330 MPa, agrees reasonably with the theoretically estimated value of 800 MPa, considering that the as deposited Li_2CO_3 contains the porous composite

structure with nanograins dispersed in the amorphous matrix that might reduce its strength.

Overall, the electrochemically deposited Li_2O exhibits much lower strength (less than 100 MPa) than that of Li_2CO_3 (~192 to ~330 MPa) but higher ductility.[36] Based on the Newman and Monroe theory, if the shear modulus of the polymer electrolyte is twice that of Li, the growth of dendrite can be inhibited.[37] This implies that if the strength of the SEI is twice higher than that of Li, the Li dendrite growth should be restrained. As the yield strength of Li is about 1 MPa from the pure mechanical perspective,[8,16,36,38] the strength of both Li_2O and Li_2CO_3 is sufficient to suppress the Li dendrite growth, which is obviously not the case.[1−11] The discrepancy may be ascribed to the fact that the Newman and Monroe model assumes the polymer electrolyte to be perfect, while the practical polymer electrolyte is never perfect. Moreover, recent experiments show that the micron sized Li rod[39] and nanometer scale Li whiskers[16,40] exhibit much higher strength than that of bulk Li.[8,16,36,38] Furthermore, there is a strong electrochemical and mechanical coupling effect during Li deposition, suggesting that a 10 mV overpotential can generate 75 MPa stress in the polymer or solid state electrolyte or SEI.[8,41] Therefore, a heuristic approach needs to be adopted to study the effect of the actual composite structure of SEI on the dendritic problem.

CONCLUSIONS

In summary, SEI related materials, Li_2CO_3 and Li_2O, were electrochemically in situ deposited in an ETEM, which were then subjected to mechanical compression. Through in situ measurements and inverse finite element simulations, it is revealed that, with the structural characteristics of nanograins dispersed in the amorphous matrix, both electrochemically deposited Li_2CO_3 and Li_2O exhibit good plasticity. The ultimate strength of Li_2CO_3 ranges from 192 to 330 MPa, while the Li_2O shows strength of less than 100 MPa, which is much weaker than that of Li_2CO_3. These results provide a new understanding of the mechanical behavior of SEI materials, which may provide important insights into the dendritic problems in LIBs.

ASSOCIATED CONTENT

TEM images of growth, compression, and tensile tests of the Li_2CO_3 and Li_2O nanorods; the SAED and EELS of the Li_2CO_3 and Li_2O nanorods; the growth rate−time plot of the Li_2CO_3 and Li_2O nanorods; force−deformation data corresponding to the compression of the Li_2CO_3 and Li_2O nanorods; inverse finite element simulation derived stress−strain data for the Li_2CO_3 and Li_2O nanorods (PDF)

In situ TEM movie showing the growth of a Li_2CO_3 nanorod (corresponding to Figure 1). The Li_2CO_3 grew directly along the CNT. The movie was recorded at 5 frames/s in TEM bright field images and played at 312× speed (AVI)

In situ TEM movie showing the growth of a Li_2CO_3 nanorod (corresponding to Figure S1). The Li_2CO_3 grew directly along the CNT. The movie was recorded at 5 frames/s in TEM bright field images and played at 84× speed (AVI)

In situ TEM movie showing the compression of a Li_2CO_3 nanorod (corresponding to Figure 2). The movie was recorded at 5 frames/s in TEM bright field images and played at 12× speed (AVI)

In situ TEM movie showing the compression experiment of a Li_2CO_3 nanorod (corresponding to Figure S3). The movie was recorded at 5 frames/s in TEM bright field images and played at 5× speed (AVI)

In situ TEM movie showing the growth of a Li_2O nanorod (corresponding to Figure S6). The Li_2O grew directly along the CNT. The movie was recorded at 5 frames/s in TEM bright field images and played at 34× speed (AVI)

In situ TEM movie showing the compression of a Li_2O nanorod (corresponding to Figure 3a). The movie was recorded at 5 frames/s in TEM bright field images and played at 22× speed (AVI)

In situ TEM movie showing the compression of a Li_2O nanotube (corresponding to Figure 3e). The movie was recorded at 5 frames/s in TEM bright field images and played at 30× speed (AVI)

AUTHOR INFORMATION

Corresponding Authors

Yongfu Tang − *Clean Nano Energy Center, State Key Laboratory of Metastable Materials Science and Technology, Yanshan University, Qinhuangdao 066004, China; Hebei Key Laboratory of Applied Chemistry, College of Environmental and Chemical Engineering, Yanshan University, Qinhuangdao 066004, China*; Email: tangyongfu@ysu.edu.cn

Liqiang Zhang − *Clean Nano Energy Center, State Key Laboratory of Metastable Materials Science and Technology, Yanshan University, Qinhuangdao 066004, China*; Email: lqzhang@ysu.edu.cn

Hui Yang − *Department of Mechanics, School of Aerospace Engineering, Huazhong University of Science and Technology, Wuhan, Hubei 430074, China*; orcid.org/0000 0002 2628 4676; Email: huiyang2017@hust.edu.cn

Jianyu Huang − *Clean Nano Energy Center, State Key Laboratory of Metastable Materials Science and Technology, Yanshan University, Qinhuangdao 066004, China; Key Laboratory of Low Dimensional Materials and Application Technology of Ministry of Education, School of Materials Science and Engineering, Xiangtan University, Xiangtan, Hunan 411105, China*; orcid.org/0000 0002 8424 5368; Email: jyhuang8@hotmail.com

Authors

Hongjun Ye − *Clean Nano Energy Center, State Key Laboratory of Metastable Materials Science and Technology, Yanshan University, Qinhuangdao 066004, China*

Siwei Gui − *Department of Mechanics, School of Aerospace Engineering, Huazhong University of Science and Technology, Wuhan, Hubei 430074, China*

Zaifa Wang − *Clean Nano Energy Center, State Key Laboratory of Metastable Materials Science and Technology, Yanshan University, Qinhuangdao 066004, China*

Jingzhao Chen − *Clean Nano Energy Center, State Key Laboratory of Metastable Materials Science and Technology, Yanshan University, Qinhuangdao 066004, China*

Qiunan Liu − *Clean Nano Energy Center, State Key Laboratory of Metastable Materials Science and Technology, Yanshan University, Qinhuangdao 066004, China*
Xuedong Zhang − *Key Laboratory of Low Dimensional Materials and Application Technology of Ministry of Education, School of Materials Science and Engineering, Xiangtan University, Xiangtan, Hunan 411105, China*
Peng Jia − *Clean Nano Energy Center, State Key Laboratory of Metastable Materials Science and Technology, Yanshan University, Qinhuangdao 066004, China*
Yushu Tang − *Institute of Nanotechnology, Karlsruhe Institute of Technology, Eggenstein Leopoldshafen 76344, Germany*
Tingting Yang − *Clean Nano Energy Center, State Key Laboratory of Metastable Materials Science and Technology, Yanshan University, Qinhuangdao 066004, China*
Congcong Du − *Clean Nano Energy Center, State Key Laboratory of Metastable Materials Science and Technology, Yanshan University, Qinhuangdao 066004, China*
Lin Geng − *Clean Nano Energy Center, State Key Laboratory of Metastable Materials Science and Technology, Yanshan University, Qinhuangdao 066004, China*
Hui Li − *Clean Nano Energy Center, State Key Laboratory of Metastable Materials Science and Technology, Yanshan University, Qinhuangdao 066004, China*
Qiushi Dai − *Clean Nano Energy Center, State Key Laboratory of Metastable Materials Science and Technology, Yanshan University, Qinhuangdao 066004, China*

Author Contributions

H.Y. and S.G. contributed equally to this work. Yo.T., L.Z., and J.H. conceived and designed the project. H.Y., Z.W., J.C., Q.L., P.J., Yu.T., and T.Y. carried out the ETEM experiments. H.Y. and S.G. carried out the finite element simulation. X.Z., C.D., L.G., H.L., and Q.D. fabricated the samples. Yo.T., L.Z., Hui Y., and J.H. supervised the experiments. Hui Y. and J.H. co wrote the paper. All authors have given approval to the final version of the manuscript.

Notes

The authors declare no competing financial interest.

■ ACKNOWLEDGMENTS

This work was financially supported by the National Natural Science Foundation of China (Nos. 51971245, 52022088, 51772262, 21406191, U20A20336, 21935009, 12172143), Beijing Natural Science Foundation (2202046), Fok Ying Tong Education Foundation of China (No. 171064), Natural Science Foundation of Hebei Province (Nos. F2021203097, B2020203037, B2018203297), and the Hunan Innovation Team (2018RS3091).

■ REFERENCES

(1) Peled, E. The Electrochemical Behavior of Alkali and Alkaline Earth Metals in Nonaqueous Battery Systems The Solid Electrolyte Interphase Model. *J. Electrochem. Soc.* **1979**, *126*, 2047−2051.
(2) Peled, E.; Menkin, S. Review SEI: Past, Present and Future. *J. Electrochem. Soc.* **2017**, *164*, A1703−A1719.
(3) Aurbach, D. Review of Selected Electrode Solution Interactions Which Determine the Performance of Li and Li Ion Batteries. *J. Power Sources.* **2000**, *89*, 206−218.
(4) Winter, M. The Solid Electrolyte Interphase The Most Important and the Least Understood Solid Electrolyte in Recharge able Li Batteries. *Z. Phys. Chem.* **2009**, *223*, 1395−1406.
(5) Wang, A.; Kadam, S.; Li, H.; Shi, S.; Qi, Y. Review on Modeling of the Anode Solid Electrolyte Interphase (SEI) for Lithium ion Batteries. *npj Comput. Mater.* **2018**, *4*, No. 15.
(6) Verma, P.; Maire, P.; Novák, P. A Review of the Features and Analyses of the Solid Electrolyte Interphase in Li ion Batteries. *Electrochim. Acta* **2010**, *55*, 6332−6341.
(7) Xu, W.; Wang, J.; Ding, F.; Chen, X.; Nasybulin, E.; Zhang, Y.; Zhang, J. G. Lithium Metal Anodes for Rechargeable Batteries. *Energy Environ. Sci.* **2014**, *7*, 513−537.
(8) Tang, Y.; Zhang, L.; Chen, J.; Sun, H.; Yang, T.; Liu, Q.; Huang, Q.; Zhu, T.; Huang, J. Electro Chemo Mechanics of Lithium in Solid State Lithium Metal Batteries. *Energy Environ. Sci.* **2021**, *14*, 602−642.
(9) Liu, W.; Liu, P.; Mitlin, D. Solid Electrolyte Interphases: Review of Emerging Concepts in SEI Analysis and Artificial SEI Membranes for Lithium, Sodium, and Potassium Metal Battery Anodes. *Adv. Energy Mater.* **2020**, *10*, No. 2002297.
(10) Liu, W.; Liu, P.; Mitlin, D. Tutorial Review on Structure Dendrite Growth Relations in Metal Battery Anode Supports. *Chem. Soc. Rev.* **2020**, *49*, 7284−7300.
(11) Whittingham, M. S. Lithium Batteries: 50 Years of Advances to Address the Next 20 Years of Climate Issues. *Nano Lett.* **2020**, *20*, 8435−8437.
(12) Bhattacharya, S.; Riahi, A. R.; Alpas, A. T. Electrochemical Cycling Behaviour of Lithium Carbonate (Li2CO3) Pre treated Graphite Anodes SEI Formation and Graphite Damage Mechanisms. *Carbon* **2014**, *77*, 99−112.
(13) Woodford, W. H.; Carter, W. C.; Chiang, Y. M. Design Criteria for Electrochemical Shock Resistant Battery Electrodes. *Energy Environ. Sci.* **2012**, *5*, 8014−8024.
(14) Li, N. W.; Shi, Y.; Yin, Y. X.; Zeng, X. X.; Li, J. Y.; Li, C. J.; Wan, L. J.; Wen, R.; Guo, Y. G. A Flexible Solid Electrolyte Interphase Layer for Long Life Lithium Metal Anodes. *Angew. Chem., Int. Ed.* **2018**, *57*, 1505−1509.
(15) Wan, J.; Hao, Y.; Shi, Y.; Song, Y. X.; Yan, H. J.; Zheng, J.; Wen, R.; Wan, L. J. Ultra Thin Solid Electrolyte Interphase Evolution and Wrinkling Processes in Molybdenum Disulfide Based Lithium ion Batteries. *Nat. Commun.* **2019**, *10*, No. 3265.
(16) Zhang, L.; Yang, T.; Du, C.; Liu, Q.; Tang, Y.; Zhao, J.; Wang, B.; Chen, T.; Sun, Y.; Jia, P.; Li, H.; Geng, L.; Chen, J.; Ye, H.; Wang, Z.; Li, Y.; Sun, H.; Li, X.; Dai, Q.; Tang, Y.; Peng, Q.; Shen, T.; Zhang, S.; Zhu, T.; Huang, J. Lithium Whisker Growth and Stress Generation in an In Situ Atomic Force Microscope Environmental Transmission Electron Microscope Set Up. *Nat. Nanotechnol.* **2020**, *15*, 94−98.
(17) Yang, T.; Jia, P.; Liu, Q.; Zhang, L.; Du, C.; Chen, J.; Ye, H.; Li, X.; Li, Y.; Shen, T.; Tang, Y.; Huang, J. Air Stable Lithium Spheres Produced by Electrochemical Plating. *Angew. Chem., Int. Ed.* **2018**, *57*, 12750−12753.
(18) Duan, H.; Chen, W. P.; Fan, M.; Wang, W. P.; Yu, L.; Tan, S. J.; Chen, X.; Zhang, Q.; Xin, S.; Wan, L. J.; Guo, Y. G. Building an Air Stable and Lithium Deposition Regulable Garnet Interface from Moderate Temperature Conversion Chemistry. *Angew. Chem., Int. Ed.* **2020**, *59*, 12069−12075.
(19) Jia, P.; Yu, M.; Zhang, X.; Yang, T.; Zhu, D.; Shen, T.; Zhang, L.; Tang, Y.; Huang, J. In situ Imaging the Electrochemical Reactions of Li CO2 Nanobatteries at High Temperatures in an Aberration Corrected Environmental Transmission Electron Microscope *Nano Res.* 2021, DOI: 10.1007/s12274 021 3514 9.
(20) Yang, T.; Li, H.; Chen, J.; Ye, H.; Yao, J.; Su, Y.; Guo, B.; Peng, Z.; Shen, T.; Tang, Y.; Zhang, L.; Huang, J. In Situ Imaging Electrocatalytic CO2 Reduction and Evolution Reactions in All Solid State Li CO2 Nanobatteries. *Nanoscale* **2020**, *12*, 23967−23974.
(21) Liu, Q.; Zhang, L.; Sun, H.; Geng, L.; Li, Y.; Tang, Y.; Jia, P.; Wang, Z.; Dai, Q.; Shen, T.; Tang, Y.; Zhu, T.; Huang, J. In Situ Observation of Sodium Dendrite Growth and Concurrent Mechanical Property Measurements Using an Environmental Transmission

Electron Microscopy Atomic Force Microscopy (ETEM AFM) Platform. *ACS Energy Lett.* **2020**, *5*, 2546−2559.
(22) Xia, C.; Kwok, C. Y.; Nazar, L. F. A High Energy Density Lithium Oxygen Battery Based on a Reversible Four Electron Conversion to Lithium Oxide. *Science* **2018**, *361*, 777−781.
(23) Luo, L.; Liu, B.; Song, S.; Xu, W.; Zhang, J. G.; Wang, C. Revealing the Reaction Mechanisms of Li O2 Batteries Using Environmental Transmission Electron Microscopy. *Nat. Nanotechnol.* **2017**, *12*, 535−539.
(24) Chen, Y.; Wang, Z.; Li, X.; Yao, X.; Wang, C.; Li, Y.; Xue, W.; Yu, D.; Kim, S. Y.; Yang, F.; Kushima, A.; Zhang, G.; Huang, H.; Wu, N.; Mai, Y. W.; Goodenough, J. B.; Li, J. Li Metal Deposition and Stripping in a Solid State Battery Via Coble Creep. *Nature* **2020**, *578*, 251−255.
(25) Bagley, E. B. Hooke's Law in Shear and Polymer Melt Fracture. *J. Appl. Phys.* **1960**, *31*, 1126−1127.
(26) Lru, D. R.; Williams, D. B. The Electron Energy Loss Spectrum of Lithium Metal. *Philos. Mag. B* **1986**, *53*, L123−L128.
(27) Wang, F.; Graetz, J.; Moreno, M. S.; Ma, C.; Wu, L.; Volkov, V.; Zhu, Y. Chemical Distribution and Bonding of Lithium in Intercalated Graphite: Identification with Optimized Electron Energy Loss Spectroscopy. *ACS Nano* **2011**, *5*, 1190−1197.
(28) Zheng, H.; Liu, Y.; Mao, S. X.; Wang, J.; Huang, J. Y. Beam Assisted Large Elongation of In Situ Formed Li2O Nanowires. *Sci. Rep.* **2012**, *2*, No. 542.
(29) Liu, X. H.; Zheng, H.; Zhong, L.; Huang, S.; Karki, K.; Zhang, L. Q.; Liu, Y.; Kushima, A.; Liang, W. T.; Wang, J. W.; Cho, J. H.; Epstein, E.; Dayeh, S. A.; Picraux, S. T.; Zhu, T.; Li, J.; Sullivan, J. P.; Cumings, J.; Wang, C.; Mao, S. X.; Ye, Z. Z.; Zhang, S.; Huang, J. Y. Anisotropic Swelling and Fracture of Silicon Nanowires during Lithiation. *Nano Lett.* **2011**, *11*, 3312−3318.
(30) Yu, M. F.; Lourie, O.; Dyer, M. J.; Moloni, K.; Kelly, T. F.; Ruoff, R. S. Strength and Breaking Mechanism of Multiwalled Carbon Nanotubes Under Tensile Load. *Science* **2000**, *287*, 637−640.
(31) Johnson, C. E.; Kummerer, K. R.; Roth, E. Ceramic breeder materials. *J. Nucl. Mater.* **1988**, *155−157*, 188−201.
(32) Billone, M. C.; Liu, Y. Y.; Poeppel, R. B.; Routbort, J. L.; Goretta, K. C.; Kupperman, D. S. Elastic and Creep Properties of Li2O. *J. Nucl. Mater.* **1986**, *141−143*, 282−288.
(33) Ebrahiminia, M.; Hooper, J. B.; Bedrov, D. Structural, Mechanical, and Dynamical Properties of Amorphous Li2CO3 from Molecular Dynamics Simulations. *Crystals* **2018**, *8*, No. 473.
(34) Shin, H.; Park, J.; Han, S.; Sastry, A. M.; Lu, W. Component / Structure Dependent Elasticity of Solid Electrolyte Interphase Layer in Li ion Batteries: Experimental and Computational Studies. *J. Power Sources* **2015**, *277*, 169−179.
(35) Pugh, S. F. XCII Relations Between the Elastic Moduli and the Plastic Properties of Polycrystalline Pure Metals. *London, Edinburgh Dublin Philos. Mag. J. Sci.* **1954**, *45*, 823−843.
(36) Masias, A.; Felten, N.; Garcia Mendez, R.; Wolfenstine, J.; Sakamoto, J. Elastic, Plastic, and Creep Mechanical Properties of Lithium Metal. *J. Mater. Sci.* **2019**, *54*, 2585−2600.
(37) Monroe, C.; Newman, J. Dendrite Growth in Lithium/Polymer Systems. *J. Electrochem. Soc.* **2003**, *150*, No. A1377.
(38) Fincher, C. D.; Ojeda, D.; Zhang, Y.; Pharr, G. M.; Pharr, M. Mechanical Properties of Metallic Lithium: from Nano to Bulk Scales. *Acta Mater.* **2020**, *186*, 215−222.
(39) Xu, C.; Ahmad, Z.; Aryanfar, A.; Viswanathan, V.; Greer, J. R. Enhanced Strength and Temperature Dependence of Mechanical Properties of Li at Small Scales and Its Implications for Li Metal Anodes. *Proc. Natl. Acad. Sci. U.S.A.* **2017**, *114*, 57−61.
(40) He, Y.; Ren, X.; Xu, Y.; Engelhard, M. H.; Li, X.; Xiao, J.; Liu, J.; Zhang, J. G.; Xu, W.; Wang, C. Origin of Lithium Whisker Formation and Growth Under Stress. *Nat. Nanotechnol.* **2019**, *14*, 1042−1047.
(41) Porz, L.; Swamy, T.; Sheldon, B. W.; Rettenwander, D.; Frömling, T.; Thaman, H. L.; Berendts, S.; Uecker, R.; Carter, W. C.; Chiang, Y. M. Mechanism of Lithium Metal Penetration through Inorganic Solid Electrolytes. *Adv. Energy Mater.* **2017**, *7*, No. 1701003.